Alternative probe chemistries for single-molecule analysis of long non-coding RNA

Authors
Kalika R. Pai[1], Aimee M. Martin[2], Julia R. Widom[1,3]*
[1]Department of Chemistry and Biochemistry, University of Oregon, Eugene, OR 97403
[2]Department of Biology, Loyola University New Orleans, New Orleans, LA 70118
[3]Oregon Center for Optical, Molecular and Quantum Science, University of Oregon, Eugene, OR 97403
*To whom correspondence should be addressed: jwidom@uoregon.edu

Running title
Probe chemistry for single-molecule analysis of RNA

Keywords
Biophysics, long non-coding RNA, nucleic acid structure, nucleic acid, RNA, RNA structure, single-molecule biophysics

Abstract
Single-molecule microscopy has been widely used to study the structure and dynamics of RNA, but extension to larger systems such as long noncoding RNA (lncRNA) has proven challenging. The length and complex nature of lncRNA limits the techniques that can be readily used to study these aspects, but methods such as single-molecule kinetic analysis of RNA transient structure (SiM-KARTS), where the binding of a short, complementary oligonucleotide probe is used to determine accessibility of a specific region of the RNA, are promising. However, adapting SiM-KARTS to systems as complex as lncRNA requires careful optimization of experimental variables that have not been thoroughly explored. In this work, SiM-KARTS, thermal denaturation experiments, and circular dichroism spectroscopy were used to analyze the binding behaviors of probes with alternative backbone chemistries, specifically DNA with locked nucleic acid residues incorporated and morpholinos. A segment of lncRNA that enabled control over the accessibility of the target sequence was used as a model. We show that optimizing probe backbone chemistry can allow for more precise distinction between different structures of the target RNA, and for fine-tuning of probe binding stability without the structural impacts that other variables such as ionic concentration may have. These results provide design principles for the application of SiM-KARTS to target RNAs of increased complexity such as lncRNA.

Introduction

Long non-coding RNAs (lncRNAs) are RNAs that do not encode protein and are greater than 200 nucleotides in length. lncRNAs perform a variety of biological functions through interactions with DNA, RNA, or proteins. Specifically, many lncRNAs have regulatory functions, either epigenetic (1), transcriptional (2), or post-transcriptional (3). Structure is an important factor in mediating the interactions that allow for these regulatory functions (4). Additionally, many lncRNAs have been found to play roles in human disease, making the molecular details of lncRNAs interesting for the potential development of therapeutics (5–7). However, there have not been in depth studies of the structure or dynamics of most lncRNAs (8), which are difficult to study due to their large size and the resulting complexity of structure.

Single-molecule methods have strong potential for investigating the structure and dynamics of lncRNAs. Specifically, single-molecule microscopy avoids ensemble averaging and allows for the investigation of the dynamics of heterogeneous systems on time scales relevant to large structural rearrangements (9). However, common techniques such as single-molecule Förster resonance energy transfer (smFRET) (10) are difficult to adapt to lncRNAs due to their length and structural complexity. For example, performing site-specific labeling of the RNA of interest can be costly, can require complex experimental workflows, and may impact the structures being studied.

An alternative to smFRET is single-molecule analysis of RNA transient structure (SiM-KARTS), which utilizes a short, fluorescently-labeled oligonucleotide probe that is complementary to a region of interest on the RNA (11–13). By tracking binding and dissociation of this probe, the accessibility of the region of interest can be revealed. For example, frequent observation of probe binding indicates high accessibility, implying a single-stranded local structure. SiM-KARTS can also be used to investigate conformational changes of RNA. Using spike train analysis (14), “bursts” of probe binding can be distinguished from random events, uncovering transitions between conformations in which the target sequence is more or less accessible for probe binding. SiM-KARTS has so far been primarily utilized to study riboswitches. For example, SiM-KARTS was performed on mRNA containing the $preQ_1$ riboswitch using a DNA probe complementary to the Shine-Dalgarno (SD) sequence (termed an “anti-SD” probe) to monitor ligand-induced pseudoknot docking (11). It was determined that there are dynamic fluctuations in the accessibility of the target sequence, even at saturating ligand concentrations. In the case of the $preQ_1$ riboswitch, techniques such as small angle x-ray scattering, smFRET, and molecular dynamics simulations aided in experimental design (15, 16).

SiM-KARTS shows promise as a method for probing lncRNA as it removes the requirement for site-specific labeling. The RNA can instead be transcribed and then end-labeled using established chemistry performed under native conditions (17, 18), or a labeled capture oligonucleotide can be utilized to localize immobilized molecules without any modification to the RNA. Previous reports of SiM-KARTS all utilized an anti-SD probe, exploiting the presence of this motif in multiple riboswitches (19–21). For lncRNA, no such common motif exists, and multiple structural domains may be of interest. For this reason, to adapt SiM-KARTS for applications to lncRNA, designing an appropriate probe is of high importance. Challenges in probe design include ensuring binding is strong enough to yield clear optical signals, yet transient enough to pose minimal disruption to the target RNA’s dynamics. Lengthening the probe can increase binding stability, but also limits the precision with which specific regions of interest can be probed and increases the potential for the probe to disrupt the structure of the RNA.

One solution to fine-tune probe binding strength without changing the length or identity of a target site is to consider alternative probe chemistries. Specifically, the incorporation of locked nucleic acid (LNA) residues into DNA is known to increase the melting temperatures of its hybrids with RNA and DNA (22). Incorporating one or two LNA residues into a SiM-KARTS probe can raise its predicted melting temperature by multiple degrees celsius, depending on placement within the strand. The binding strength of short sequences can also be increased by the use of morpholino oligonucleotides, typically used as gene knockdown reagents due to their high binding specificity and stability (23). Mono- and divalent cations are well known to increase melting temperatures of DNA and RNA duplexes and hybrids (24), making adjusting cation concentrations a possible avenue for optimizing probe binding stability. However, as ionic conditions also have a large impact on stability of RNA secondary and tertiary structure (25), controlling probe binding stability in this manner could distort the structure of the RNA being studied.

In this study, we investigated the impact of probe chemistry and ionic conditions on the binding behavior of SiM-KARTS probes in different structural contexts using a model RNA based on the lncRNA *Braveheart* (Bvht; Fig. 1A) (26–28). We show that probes with LNA residues incorporated demonstrate improved structural sensitivity over DNA alone, while morpholino probes show little structural sensitivity. Additionally, we demonstrate that changes in the ionic environment can produce non-monotonic changes in probe binding, likely due to competing effects on the structure of the target RNA and the binding stability of the probe. These results will guide probe design for future studies utilizing SiM-KARTS, including investigations of lncRNA structure and dynamics.

Results

Experimental Design

A 59-nucleotide sequence containing helix 9 of Bvht (hereafter called “Bvht H9”) was selected from the full-length RNA as a model for which different structures could be obtained by hybridizing complementary RNA oligonucleotides (Fig. 1A, sequences in Table 1). The native structure of Bvht, as previously determined by chemical probing, contains a flexible, single-stranded region to the 5’ side of H9 (26, 28). Using RNAstructure (29), we found that outside the context of the full-length RNA, Bvht H9 is predicted to fold into a structure containing 2 hairpin loops. An 8-nucleotide segment of one loop was chosen as the probe binding site (Fig. 1A). The sequence of this loop is unique within the entirety of Bvht, so this probing site could be feasible for studies using the full lncRNA. The complementary strand “cs” was designed to generate a 9-nucleotide single-stranded region around the probing site upon hybridization to Bvht H9, and the blocking strand “bs” was designed to sequester the probing region in double-stranded form (Fig. 1A). Molecules were detected using prism-based total internal reflection fluorescence (TIRF) microscopy, with Bvht H9 detected in the green emission channel via a Cy3 label on its 3’ end or the 3’ end of cs or bs (ensuring that only hybridized molecules were detected in those cases), and 5’ Cy5- or TYE665-labeled probe detected in the red channel (Fig. 1B). Probes were complementary to the 8-nucleotide target sequence and included one with a fully DNA backbone (“DNA”), one with an LNA residue at position 2 (“LNA2”), one with LNA residues at positions 2 and 3 (“LNA23”) and one with a morpholino backbone (“MO”) (Fig. 1C-E). These probe chemistries were selected to achieve a range of melting temperatures of the probe:RNA hybrid. Fluorescence intensity traces from the red (probe) channel were idealized using hidden Markov modeling to define probe-bound and probe-unbound states (Fig. 1C-E). Ideal probe concentration was determined to be 60 nM by

analyzing SiM-KARTS data collected with 20-100 nM LNA2 and comparing changes in bound and unbound dwell times (Fig. S1).

SiM-KARTS probe chemistry impacts RNA binding properties

We investigated the impact of probe chemistry on binding behavior to Bvht H9 (containing a partially occluded probe binding site) and Bvht H9:cs (containing a single-stranded probe binding site). The ideal probe will bind in a manner sensitive to structure, and have bound dwell times that are long enough to be readily distinguished from background noise, yet not so long that the binding impacts the structure of the target RNA. The rates of probe binding and dissociation were quantified using cumulative distribution curves (Fig. 2), which show the probability that a bound or unbound segment of a trace has a duration less than or equal to the corresponding time indicated on the x-axis. A slower rise from zero to 1 for unbound dwells indicates that longer times between binding events are typical. Similarly, for bound dwells, a slower rise from zero to 1 indicates that longer binding events are typical. The unbound dwell times differ for each combination of target RNA structure (Bvht H9 or Bvht H9:cs) and probe chemistry (DNA, LNA2, LNA23 or MO) (Fig. 2, Table 2). Unbound dwell times are longer in the presence of 1 mM Mg^{2+} for DNA, LNA2 and LNA23 binding to Bvht H9:cs, while Mg^{2+} has little impact on binding to Bvht H9, or on binding of MO to either structure. The DNA probe generally has the longest unbound dwell times across all conditions, though the unbound dwell times for DNA and LNA2 probing Bvht H9 are very similar. LNA2 consistently binds Bvht H9:cs more quickly than Bvht H9, showing strong discrimination between the two structures in both the absence and presence of 1 mM Mg^{2+}. LNA23 likewise exhibits faster binding to Bvht H9:cs than Bvht H9 in 0 mM Mg^{2+}, but has opposite behavior at 1 mM Mg^{2+}. Experiments with Bvht H9:bs probed by LNA2 and MO show significantly fewer binding events per trace and longer unbound dwell times compared to Bvht H9 and Bvht H9:cs (Fig. S2, Table S1), confirming that probe binding is strongly inhibited by complete occlusion of the probe binding site.

The precision of this approach was quantified by comparing dwell times extracted from multiple movies collected on the same day, multiple movies collected across different days (Fig. S3A-B; Table S2), and batches of traces (termed bootstrapped sets) selected randomly from within the combined data (Fig. S3C-D; Table S3) (data on LNA2 binding to Bvht H9:cs). A small amount of variation in unbound and bound dwells is observed in data collected on the same day (Fig. S3A,B), with both quantities differing by 6-7% (standard deviation divided by mean) across movies on the day with higher variability (Table S2). Comparable variation of ~5% in unbound dwells was observed across bootstrapped sets (Table S3). In contrast, systematic variation of unbound dwell times is seen in the case of data collected on separate days, with a difference of 32% (difference divided by mean) between data pooled from movies on each day. This is likely due to inconsistencies in probe concentration and degradation from freeze-thaw cycles. In the results reported herein, all data for a given probe was collected on the same day to ensure accurate comparisons between target RNA structures and ionic conditions, except for MO, for which differences in unbound dwells should not be necessarily considered significant.

It is apparent that the increasing inclusion of LNA residues leads to longer bound dwell times, particularly with the target Bvht H9:cs (Fig. 2B,D; Table 2). There is also distinct separation between the bound dwell times of LNA probes for different RNA structures, with longer bound times observed for Bvht H9:cs, which has a more accessible binding site, than Bvht H9. Comparatively, the bound dwell times for the DNA and MO probes do not discriminate between structures as effectively. Interestingly, for all probes except MO, the cumulative distributions of bound dwells for Bvht H9:cs are best described with a double-exponential fit, while bound dwells for Bvht H9 can be adequately described using a single exponential. In these cases, the dominant component of a double-exponential fit (as reported for all bound dwells herein) has a

weight of nearly 100%. This distinction between target RNA structures is most evident with the LNA probes, where the heavier component is weighted at 99-100% for Bvht H9, with a range from 51-62% for Bvht H9:cs (Table 2). The DNA probe exhibits the same trend but has a less drastic difference between structures, with 100% in the dominant component for Bvht H9 and 81-88% for Bvht H9:cs.

Probe melting temperatures

As an orthogonal metric of binding stability, thermal denaturation experiments were performed for each probe type bound to Bvht H9 34-45, a short RNA containing the probing sequence with 2-nucleotide overhangs on either end (Fig. 3). Melting curves were recorded in the absence or presence of 1 mM Mg^{2+} by monitoring absorbance at 260 nm, and were fitted to extract melting temperatures (T_M) (Fig. S4). As expected, the DNA probe has the lowest T_M, and the T_M values of LNA probes increase with the number of LNA residues incorporated (Table 3). The morpholino probe is similar in melting behavior to LNA2, but shows lower sensitivity to Mg^{2+}. The T_M obtained for the DNA probe represents an upper limit, as the slope of the melting curve indicates that the probe does not fully hybridize to the RNA even at 0 °C. The T_M values of probe hybrids with Bvht H9 34-45 follow the same trends as the bound dwells of probes binding to Bvht H9:cs observed by SiM-KARTS, with higher T_M (Table 3) associated with longer bound dwell time (Table 2). Interestingly, the measured T_M values for LNA probes are significantly higher than their estimated values from IDT OligoAnalyzer (30–33). However, the model used by that calculator is experimentally parameterized only for LNA:DNA hybrids, not LNA:RNA, and our results more closely approximate the predictions for LNA:DNA (Table 3). Additionally, no such melting temperature calculator exists for morpholinos, with most studies of morpholino-nucleic acid hybrids being limited to interactions with DNA only (34, 35). However, the MO:RNA hybrids that have been studied were shown to have higher T_M values than corresponding DNA:RNA hybrids by nearly 10 °C (36), which is consistent with the MO:RNA melting temperatures measured here.

Controlling binding via ionic concentration

The changes in T_M observed with and without 1 mM Mg^{2+} show a clear relationship between divalent cation concentration and probe:RNA hybrid stability. To investigate the impact of ionic conditions in SiM-KARTS, we chose to further study the binding of LNA2, as it showed promise as a more stably-binding and more structure-sensitive probe than DNA (Fig. 4, Table 4). The unbound dwell times for the more accessible Bvht H9:cs increase as Mg^{2+} concentration increases, with the less accessible Bvht H9 having consistent unbound dwell times regardless of Mg^{2+} concentration (Fig. 4A). Unbound and unbound dwell times display little dependence on Na^{+} concentration for either target RNA (Fig. 4C-D). Bound dwells for Bvht H9 are short regardless of Mg^{2+} or Na^{+} concentration (Table 4). Bound dwells lengthen for Bvht H9:cs between 0 and 1 mM Mg^{2+}, but shorten substantially with the addition of 20 mM Mg^{2+}, which has previously been used for SiM-KARTS (11). Additionally, the faster component of the double-exponential fit for Bvht H9:cs increases significantly in weight at 20 mM Mg^{2+} (Table 4). This suggests that at high concentrations, Mg^{2+} is no longer just stabilizing the interaction between Bvht H9:cs and LNA2, but may be impacting the overall structure of Bvht H9:cs, affecting the accessibility of the probe binding site.

To further understand the impact of Mg^{2+} concentration on the nature of the binding site encountered by a probe, circular dichroism (CD) spectroscopy was performed on Bvht H9 34-45 and Bvht H9:cs at 0, 1, and 20 mM Mg^{2+}. Differences in the structure of Bvht H9 34-45 can be seen in the presence and absence of Mg^{2+}, but there are no appreciable differences between 1 mM and 20 mM Mg^{2+} (Fig. 5A). The lineshape of the CD spectrum of Bvht H9:cs remains

consistent across Mg^{2+} concentrations, indicating that Mg^{2+} does not induce changes in its global architecture (Fig. 5B). However, the magnitude of the CD signal increases continuously with increasing Mg^{2+}, suggesting that this assembly adopts a more ordered structure in the presence of Mg^{2+}. This ordered structure may poise the target site in a configuration that is not amenable to probe binding, explaining the slower binding and more rapid dissociation observed at 20 mM Mg^{2+}.

The binding of the morpholino probe was also of particular interest, as its neutral backbone could limit the effect that ions have on probe binding. Here, some variation is seen in the length of unbound dwells, without a clear trend between dwell time and structure probed or salt concentration (Fig. 6, Table 5). The bound dwells are of consistent length and the fit components are of consistent weight for MO binding to Bvht H9 and Bvht H9:cs under all ionic conditions tested. This suggests that the binding stability of the morpholino probe is indeed less sensitive to ionic conditions, but, as noted earlier, is also less sensitive to the structure of the target RNA.

Discussion

RNA studies using SiM-KARTS have been limited to date, in part due to the optimization necessary to yield clear, interpretable signals from probe binding events. In this work, we found that probes with backbone chemistries beyond DNA can successfully report on RNA structure via SiM-KARTS. Specifically, we found that the incorporation of LNA residues in a DNA oligonucleotide leads to clearer discrimination between target RNA structures in which the probe binding sites exhibit different levels of accessibility. For LNA probes, bound dwell times were notably longer when probing a region that is fully single-stranded and accessible (as in Bvht H9:cs), than they were when probing a partially occluded region (as in Bvht H9). Although the bound dwell times of LNA probes on partially occluded regions were comparable to those observed for LNA2 on the fully occluded Bvht H9:bs complex, the latter was distinguished by much longer unbound dwell times. SiM-KARTS measurements utilizing LNA probes can therefore effectively discriminate among fully accessible, partially occluded and fully occluded binding sites on our model RNA.

Previously, much of the interpretation of SiM-KARTS data was based on *unbound* dwell times being longer for structures with less accessible probing regions, compared to structures with more accessible regions (11–13). Interestingly, we found that this is not necessarily the case under all circumstances. In the absence of Mg^{2+}, the dependence of unbound dwell times on the structure of the target RNA was inconsistent across different probe types. Here, the DNA and MO probes demonstrated longer unbound dwells for the more accessible target RNA structure than the less accessible structure, which is contrary to typical interpretation of data. In contrast, in the presence of 1 mM Mg^{2+}, longer unbound dwells were observed for LNA and morpholino probes with the less accessible target structure than the more accessible structure, as may be expected. The unbound dwell times of the DNA probe did not adequately differentiate the two structures.

We have found that *bound* dwell times can also be used to discern information about the structure of the target RNA. There is a clear target structure-dependence of the bound dwell times when using LNA probes, with longer bound dwell times for the structure with a more accessible probe binding site in both the absence or presence of 1 mM Mg^{2+}. In the case of DNA, bound dwell times are 50-100% higher for the more accessible structure, but both are very short and are therefore difficult to distinguish from background noise. The morpholino

probe, on the other hand, exhibits no appreciable difference between structures. We found that additional information about target RNA structure can be gathered from the component weights of double-exponential fits to bound dwell time distributions. A single component is vastly dominant for DNA and LNA probes binding to more structured target RNA sites, such as Bvht H9 under all conditions and, to a lesser extent, Bvht H9:cs in 20 mM Mg^{2+}. In contrast, both components show significant weight for less structured target RNA such as Bvht H9:cs. While the exact mechanism underlying these differences is not known, it is clear that different target structures exhibit different fitting characteristics.

Previous studies with SiM-KARTS have utilized Mg^{2+} concentrations above those generally considered physiological (37), ranging from 5 to 20 mM (11, 12, 20), to aid in stabilization of probe binding. We have found that for LNA probes, adjusting divalent cation concentration impacts both bound and unbound dwell times; however the impact on bound dwell times is not monotonic as Mg^{2+} concentration increases. Addition of Mg^{2+} increases the stability of the probe:RNA hybrid, as demonstrated by measured melting temperatures, but can also lead to structural changes in the target RNA, as observed by CD. While the exact nature of these rearrangements is not known for Bvht H9, it is likely that the combination of increasing probe:RNA hybrid stability and changing structure are responsible for the non-monotonic dependence of bound dwell times on Mg^{2+} concentration. Changes in monovalent salt concentration do not lead to significant changes in bound or unbound dwells.
Based on these results, we propose that to best optimize probe binding in SiM-KARTS experiments, it is advantageous to change the probe's chemistry rather than tune binding using environmental variables such as salt conditions. Additionally, it is worthwhile to consider both bound and unbound dwell times as well as their exponential fitting characteristics, to gain maximal information about the structure of the binding site and discriminate between similar structures.

Experimental procedures

Oligonucleotides

To aid with oligonucleotide design, secondary structures of Bvht H9 alone and with potential complementary strand bound were predicted using RNAstructure (29). Bvht H9 and the complementary strands cs and bs (Table 1) were purchased from Dharmacon, with 3' Cy3 labeling for cs and bs. Bvht H9 was purchased with 5' biotin, and was 3' end-labeled with Cy3 hydrazide (Lumiprobe) following established protocols (17) for experiments performed on this RNA without any complementary strand. Probes were designed to be complementary to nucleotides 36-43 of Bvht H9, with low melting temperatures to ensure transient binding. The DNA and DNA/LNA chimera probes were purchased from IDT with 5' Cy5 (DNA) or TYE665 (LNA) labeling. All of the above oligonucleotides were HPLC-purified by the manufacturer. The morpholino probe was purchased from GeneTools with 5' sulfo-Cy5 and was purified by filtration and precipitation by the manufacturer. For melting curves and CD, a truncated version of Bvht H9 was purchased from IDT, containing only the probing region with 2-nucleotide overhangs (Bvht H9 34-45).

RNA preparation for SiM-KARTS

For single-molecule experiments, Bvht H9 was heated to 90 °C in a buffer consisting of 50 mM Tris-HCl and 100 mM NaCl at pH 7.5 for 2 minutes at 1.5 uM, or at 1 uM in the presence of equimolar cs or bs when desired. The RNA was then slowly cooled in air for 10 minutes before being placed on ice and used in experiments.

SiM-KARTS data collection

Microscope slides were cleaned and passivated using the established DDS-Tween20 method (38). Briefly, quartz slides were cleaned and coated with dichlorodimethylsilane (Sigma Aldrich), then assembled into flow cells, which were stored at 4 °C. Just prior to imaging, passivation was completed by incubating 0.2 mg/mL bBSA (ThermoFisher) for 5 minutes, 0.2% v/v Tween-20 (Sigma Aldrich) for 10 minutes, and 0.2 mg/mL streptavidin (ThermoFisher) for 5 minutes, each in a buffer consisting of 10 mM Tris-HCl and 50 mM NaCl at pH 8. RNA was flowed on at a concentration of 10 pM in a buffer consisting of 50 mM Tris-HCl and 100 mM NaCl at pH 7.5 and allowed to incubate for 5-10 minutes until an adequate density of molecules was achieved. Probes were flowed on in a buffer consisting of 50 mM Tris-HCl pH 7.5 and variable salt concentrations as specified in figures (100-500 mM NaCl and 0-20 mM $MgCl_2$), supplemented with 5 nM 3,4-dihydroxybenzoic acid (Sigma Aldrich), 5 mM Trolox (Sigma Aldrich), and 50 nM Protocatechuate 3,4-dioxygenase (MP Biomedicals) as an oxygen scavenging system. Probes were present at 60 nM unless otherwise noted. This mixture was incubated in the sample chamber for 10 minutes prior to data acquisition.

Data were collected at room temperature on a home-built prism-type total internal reflection fluorescence microscope (Leica DMi8 inverted microscope, 63x oil immersion objective). Fluorophores were excited continuously during data acquisition using a 532 nm laser (Coherent OBIS 532 LS) at 80 mW and a 637 nm laser (Coherent OBIS 637 LX) at 100 mW. Emission was split into red and green channels, which were projected side-by-side onto an Andor iXon 888 EMCCD camera. Movies were 2,000 frames in duration with an exposure time of 100 ms.

SiM-KARTS data analysis

Coordinates of RNA molecules in the green channel were identified for each video file after rolling ball background subtraction using FIJI. Custom MATLAB code was then used to extract fluorophore intensity traces for these locations and the corresponding locations in the red channel, which were identified by performing a calibration using fluorescent microspheres visible in both channels. Traces exhibiting single-step photobleaching of Cy3 were selected manually using custom MATLAB code, and data from multiple movies were combined to yield the number of traces indicated by “N” in each data table. Selected traces were placed through a Wiener filter with a range of 1 to reduce background noise. Filtered traces underwent hidden Markov modeling in QuB Software (39–43) using a 2-state model (probe bound and unbound) to obtain idealized traces. Transition rates were analyzed by obtaining the durations of dwells in the bound and unbound states.The cumulative distributions of each were fit with single- or double-exponential functions in Mathematica (Wolfram Alpha) (Eq. 1 or Eq. 2, respectively, where w_i is the weight of component i and τ_i is its time constant).

(1) $$\mathrm{Fit}(t) = w(1 - e^{-t/\tau})$$

(2) $$\mathrm{Fit}(t) = w_1(1 - e^{-t/\tau_1}) + w_2(1 - e^{-t/\tau_2})$$

Melting curves

Melting curves were recorded on a Jasco J-1500 CD spectrometer in a low headspace, 1 cm pathlength cuvette (Starna 26.100/LHS). 3 μM each of probe and Bvht H9 34-45 were combined in 20 mM sodium phosphate (pH 7.4) supplemented with NaCl to attain a total Na^+ concentration of 100 mM. Samples were incubated at 0 °C for 10 minutes before being heated at 0.2 °C/min from 0 °C to 40, with absorbance monitored at 260 nm. A buffer scan was subtracted, and the resulting curves were rescaled to run from zero to 1 for display. T_M values were obtained by fitting the curves in Mathematica, as described previously (44). T_M values were predicted using the Integrated DNA Technologies Oligo Analyzer (https://www.idtdna.com/pages/tools/oligoanalyzer) using an oligo concentration setting of 1.5

μM (following recommendations for equimolar strand concentrations) and ion concentrations to match desired conditions.

Circular dichroism spectroscopy

CD spectra were recorded on a Jasco J-1500 CD spectrometer in a 1 cm pathlength cuvette (Starna 26.100F-Q-10/Z15). Bvht H9:cs or Bvht H9 34-45 was prepared at an optical density of ~0.8 in a buffer consisting of 20 mM sodium phosphate (pH 7.4) supplemented with NaCl to attain a total Na^+ concentration of 100 mM. Bvht H9:cs was then annealed as described above. Spectra were collected from 350-195 nm at 20 °C, at a 10 nm/min scanning speed. Spectra were processed by subtracting a buffer scan, zeroing the long-wavelength baseline, and converting to Δε using Eq. 3, where CD is the CD signal in millidegrees, L is the pathlength, and C is the sample concentration determined by A260.

(3) $$\Delta\epsilon = \frac{CD}{32980 \cdot L \cdot C}$$

Data availability

Data and custom software underlying this report are available upon request to the corresponding author: jwidom@uoregon.edu

Supporting information

This article contains supporting information.

Author contributions

KRP: Conceptualization, formal analysis, investigation, methodology, visualization, writing-original draft. AMM: Formal analysis, investigation, writing - review & editing. JRW: Conceptualization, funding acquisition, project administration, supervision, writing - review & editing

Funding and additional information

This work was supported by American Heart Association grants 857651 (to JRW) and 23IAUST1029376 (to Daniel Grimes), National Institutes of Health grant R35 GM147229 (to JRW), and National Science Foundation Graduate Research Fellowship Program under Grant No. 2236419 (to KRP). The content is solely the responsibility of the authors and does not necessarily represent the official views of the National Institutes of Health. Any opinions, findings, and conclusions or recommendations expressed in this material are those of the author(s) and do not necessarily reflect the views of the National Science Foundation.

Conflict of interest

The authors declare that they have no conflicts of interest with the contents of this article.

References

1. Much, C., Lasda, E. L., Pereira, I. T., Vallery, T. K., Ramirez, D., Lewandowski, J. P., Dowell, R. D., Smallegan, M. J., and Rinn, J. L. (2024) The temporal dynamics of lncRNA Firre-mediated epigenetic and transcriptional regulation. *Nat. Commun.* **15**, 6821
2. Dykes, I. M., and Emanueli, C. (2017) Transcriptional and Post-Transcriptional Gene Regulation by Long Non-Coding RNA. *Genomics Proteomics Bioinformatics*. **15**, 177–186
3. He, R.-Z., Luo, D.-X., and Mo, Y.-Y. (2019) Emerging roles of lncRNAs in the post-transcriptional regulation in cancer. *Genes Dis.* **6**, 6–15
4. Mattick, J. S., Amaral, P. P., Carninci, P., Carpenter, S., Chang, H. Y., Chen, L.-L., Chen, R., Dean, C., Dinger, M. E., Fitzgerald, K. A., Gingeras, T. R., Guttman, M., Hirose, T., Huarte, M., Johnson, R., Kanduri, C., Kapranov, P., Lawrence, J. B., Lee, J. T., Mendell, J. T., Mercer, T. R., Moore, K. J., Nakagawa, S., Rinn, J. L., Spector, D. L., Ulitsky, I., Wan, Y., Wilusz, J. E., and Wu, M. (2023) Long non-coding RNAs: definitions, functions, challenges and recommendations. *Nat. Rev. Mol. Cell Biol.* **24**, 430–447
5. Han, P., Li, W., Lin, C.-H., Yang, J., Shang, C., Nurnberg, S. T., Jin, K. K., Xu, W., Lin, C.-Y., Lin, C.-J., Xiong, Y., Chien, H.-C., Zhou, B., Ashley, E., Bernstein, D., Chen, P.-S., Chen, H.-S. V., Quertermous, T., and Chang, C.-P. (2014) A long noncoding RNA protects the heart from pathological hypertrophy. *Nature*. **514**, 102–106
6. Jiang, Z., Yu, Q., and Luo, X. (2020) Identification of long non-coding RNA MVIH as a prognostic marker and therapeutic target in acute myeloid leukemia. *J. Clin. Lab. Anal.* **34**, e23113
7. Lu, G., and Zhang, Y. (2020) Long non-coding RNA ATB promotes human non-small cell lung cancer proliferation and metastasis by suppressing miR-141-3p. *PLOS ONE*. **15**, e0229118
8. McDonel, P., and Guttman, M. (2019) Approaches for Understanding the Mechanisms of Long Noncoding RNA Regulation of Gene Expression. *Cold Spring Harb. Perspect. Biol.* **11**, a032151
9. Lerner, E., Cordes, T., Ingargiola, A., Alhadid, Y., Chung, S., Michalet, X., and Weiss, S. (2018) Toward dynamic structural biology: Two decades of single-molecule Förster resonance energy transfer. *Science*. 10.1126/science.aan1133
10. Lai, W.-J. C., Kayedkhordeh, M., Cornell, E. V., Farah, E., Bellaousov, S., Rietmeijer, R., Salsi, E., Mathews, D. H., and Ermolenko, D. N. (2018) mRNAs and lncRNAs intrinsically form secondary structures with short end-to-end distances. *Nat. Commun.* **9**, 4328
11. Rinaldi, A. J., Lund, P. E., Blanco, M. R., and Walter, N. G. (2016) The Shine-Dalgarno sequence of riboswitch-regulated single mRNAs shows ligand-dependent accessibility bursts. *Nat. Commun.* **7**, 8976
12. Chauvier, A., Cabello-Villegas, J., and Walter, N. G. (2019) Probing RNA structure and interaction dynamics at the single molecule level. *Methods*. **162–163**, 3–11
13. Welty, R., Schmidt, A., and Walter, N. G. (2023) Probing Transient Riboswitch Structures via Single Molecule Accessibility Analysis. in *RNA Structure and Dynamics* (Ding, J., Stagno, J. R., and Wang, Y.-X. eds), pp. 37–51, Methods in Molecular Biology, Springer US, New York, NY, **2568**, 37–51
14. Gourévitch, B., and Eggermont, J. J. (2007) A nonparametric approach for detection of bursts in spike trains. *J. Neurosci. Methods*. **160**, 349–358
15. Jenkins, J. L., Krucinska, J., McCarty, R. M., Bandarian, V., and Wedekind, J. E. (2011) Comparison of a PreQ1 Riboswitch Aptamer in Metabolite-bound and Free States with Implications for Gene Regulation*. *J. Biol. Chem.* **286**, 24626–24637
16. Suddala, K. C., Rinaldi, A. J., Feng, J., Mustoe, A. M., Eichhorn, C. D., Liberman, J. A., Wedekind, J. E., Al-Hashimi, H. M., Brooks, C. L., III, and Walter, N. G. (2013) Single transcriptional and translational preQ$_1$ riboswitches adopt similar pre-folded ensembles that

follow distinct folding pathways into the same ligand-bound structure. *Nucleic Acids Res.* **41**, 10462–10475
17. Awwad, D. A., Rahmouni, A. R., and Aboul-ela, F. (2020) Protocol for efficient fluorescence 3′ end-labeling of native noncoding RNA domains. *MethodsX*. **7**, 101148
18. Chillón, I., Marcia, M., Legiewicz, M., Liu, F., Somarowthu, S., and Pyle, A. M. (2015) Native Purification and Analysis of Long RNAs. *Methods Enzymol.* **558**, 3–37
19. Chauvier, A., Dandpat, S. S., Romero, R., and Walter, N. G. (2024) A nascent riboswitch helix orchestrates robust transcriptional regulation through signal integration. *Nat. Commun.* **15**, 3955
20. Blechar, J., de Jesus, V., Fürtig, B., Hengesbach, M., and Schwalbe, H. (2024) Shine–Dalgarno Accessibility Governs Ribosome Binding to the Adenine Riboswitch. *ACS Chem. Biol.* **19**, 607–618
21. Suddala, K. C., Price, I. R., Dandpat, S. S., Janeček, M., Kührová, P., Šponer, J., Banáš, P., Ke, A., and Walter, N. G. (2019) Local-to-global signal transduction at the core of a Mn2+ sensing riboswitch. *Nat. Commun.* **10**, 4304
22. Singh, S. K., Koshkin, A. A., Wengel, J., and Nielsen, P. (1998) LNA (locked nucleic acids): synthesis and high-affinity nucleic acid recognition. *Chem. Commun.* 10.1039/a708608c
23. Karkare, S., and Bhatnagar, D. (2006) Promising nucleic acid analogs and mimics: characteristic features and applications of PNA, LNA, and morpholino. *Appl. Microbiol. Biotechnol.* **71**, 575–586
24. Nakano, S., Fujimoto, M., Hara, H., and Sugimoto, N. (1999) Nucleic acid duplex stability: influence of base composition on cation effects. *Nucleic Acids Res.* **27**, 2957–2965
25. Draper, D. E. (2004) A guide to ions and RNA structure. *RNA*. **10**, 335–343
26. Klattenhoff, C. A., Scheuermann, J. C., Surface, L. E., Bradley, R. K., Fields, P. A., Steinhauser, M. L., Ding, H., Butty, V. L., Torrey, L., Haas, S., Abo, R., Tabebordbar, M., Lee, R. T., Burge, C. B., and Boyer, L. A. (2013) Braveheart, a Long Noncoding RNA Required for Cardiovascular Lineage Commitment. *Cell*. **152**, 570–583
27. Xue, Z., Hennelly, S., Doyle, B., Gulati, A. A., Novikova, I. V., Sanbonmatsu, K. Y., and Boyer, L. A. (2016) A G-Rich Motif in the lncRNA Braveheart Interacts with a Zinc-Finger Transcription Factor to Specify the Cardiovascular Lineage. *Mol. Cell*. **64**, 37–50
28. Kim, D. N., Thiel, B. C., Mrozowich, T., Hennelly, S. P., Hofacker, I. L., Patel, T. R., and Sanbonmatsu, K. Y. (2020) Zinc-finger protein CNBP alters the 3-D structure of lncRNA Braveheart in solution. *Nat. Commun.* **11**, 148
29. Ali, S. E., Mittal, A., and Mathews, D. H. (2023) RNA Secondary Structure Analysis Using RNAstructure. *Curr. Protoc.* **3**, e846
30. Owczarzy, R., Tataurov, A. V., Wu, Y., Manthey, J. A., McQuisten, K. A., Almabrazi, H. G., Pedersen, K. F., Lin, Y., Garretson, J., McEntaggart, N. O., Sailor, C. A., Dawson, R. B., and Peek, A. S. (2008) IDT SciTools: a suite for analysis and design of nucleic acid oligomers. *Nucleic Acids Res.* **36**, W163–W169
31. Sugimoto, N., Nakano, S., Katoh, M., Matsumura, A., Nakamuta, H., Ohmichi, T., Yoneyama, M., and Sasaki, M. (1995) Thermodynamic parameters to predict stability of RNA/DNA hybrid duplexes. *Biochemistry*. **34**, 11211–11216
32. Owczarzy, R., You, Y., Moreira, B. G., Manthey, J. A., Huang, L., Behlke, M. A., and Walder, J. A. (2004) Effects of Sodium Ions on DNA Duplex Oligomers: Improved Predictions of Melting Temperatures. *Biochemistry*. **43**, 3537–3554
33. Owczarzy, R., Moreira, B. G., You, Y., Behlke, M. A., and Walder, J. A. (2008) Predicting Stability of DNA Duplexes in Solutions Containing Magnesium and Monovalent Cations. *Biochemistry*. **47**, 5336–5353
34. Gong, P., Wang, K., Liu, Y., Shepard, K., and Levicky, R. (2010) Molecular Mechanisms in Morpholino-DNA Surface Hybridization. *J. Am. Chem. Soc.* **132**, 9663–9671

35. Rihon, J., Mattelaer, C.-A., Montalvão, R. W., Froeyen, M., Pinheiro, V. B., and Lescrinier, E. (2024) Structural insights into the morpholino nucleic acid/RNA duplex using the new XNA builder Ducque in a molecular modeling pipeline. *Nucleic Acids Res.* **52**, 2836–2847
36. Summerton, J. E. (2003) Morpholinos and PNAs compared. *Lett. Pept. Sci.* **10**, 215–236
37. Leamy, K. A., Assmann, S. M., Mathews, D. H., and Bevilacqua, P. C. (2016) Bridging the Gap Between In Vitro and In Vivo RNA Folding. *Q. Rev. Biophys.* **49**, e10
38. Hua, B., Young Han, K., Zhou, R., Kim, H., Shi, X., Abeysirigunawardena, S. C., Jain, A., Singh, D., Aggarwal, V., Woodson, S. A., and Ha, T. (2014) An Improved Surface Passivation Method for Single-Molecule Studies. *Nat. Methods*. **11**, 1233–1236
39. Milescu, L. S., Nicolai, C., and Bannen, J. (2000) QuB Software
40. Nicolai, C., and Sachs, F. (2013) SOLVING ION CHANNEL KINETICS WITH THE QuB SOFTWARE. *Biophys. Rev. Lett.* **08**, 191–211
41. Qin, F., Auerbach, A., and Sachs, F. (1996) Estimating single-channel kinetic parameters from idealized patch-clamp data containing missed events. *Biophys. J.* **70**, 264–280
42. Hawkes, A. G., Jalali, A., and Colquhoun, D. (1997) The distributions of the apparent open times and shut times in a single channel record when brief events cannot be detected. *Philos. Trans. R. Soc. Lond. Ser. Phys. Eng. Sci.* **332**, 511–538
43. Qin, F., Auerbach, A., and Sachs, F. (1997) Maximum likelihood estimation of aggregated Markov processes. *Proc. R. Soc. Lond. B Biol. Sci.* **264**, 375–383
44. Hoeher, J. E., Sande, N. E., and Widom, J. R. (2024) Probing and perturbing riboswitch folding using a fluorescent base analogue. *Photochem. Photobiol.* **100**, 419–433

Abbreviations

The abbreviations used are: lncRNA, long non-coding RNA; SiM-KARTS, single-molecule kinetic analysis of RNA transient structure; smFRET, single-molecule Förster resonance energy transfer; SD, Shine Dalgarno; LNA, locked nucleic acid; MO, morpholino; Bvht, *Braveheart*; T_M, melting temperature; CD, circular dichroism.

Tables

Oligo name	Oligo type	Sequence
Bvht H9	RNA	5'Bi GAAGCAAAGCAAGUUCAAUGACCGUGCGACCUG GCUCUUGUUUGGGCCUAAGGAAAGCC
cs	RNA	GCCAGGUCGCACGGU 3'Cy3
bs	RNA	CCCAAACAAGAGCCAG 3'Cy3
Bvht H9 34-45	RNA	GCUCUUGUUUGG
DNA	DNA	5'Cy5 AAACAAGA
LNA2	DNA w/ LNA	5'TYE665 A+AACAAGA
LNA23	DNA w/ LNA	5'TYE665 A+A+ACAAGA
MO	Morpholino	sulfo-Cy5 AAACAAGA

Table 1. Sequences of oligonucleotides

		Bvht H9			Bvht H9:cs		
Probe	$[Mg^{2+}]$ (mM)	$\tau_{unbound}$ (s)	$\tau_{bound,avg}$ (s) (weight)	N	$\tau_{unbound}$ (s)	$\tau_{bound,avg}$ (s) (weight)	N
DNA	0	9.0	0.1 (1.00)	118	9.5	0.2 (0.81)	93
DNA	1	8.9	0.2 (1.00)	97	12.0	0.3 (0.88)	101
LNA2	0	9.9	0.1 (0.99)	101	3.7	0.6 (0.55)	104
LNA2	1	9.4	0.2 (1.00)	109	5.2	0.7 (0.55)	167
LNA23	0	5.8	0.2 (1.00)	124	3.9	1.3 (0.62)	157
LNA23	1	5.4	0.2 (1.00)	102	8.0	2.4 (0.51)	109
MO	0	2.8	0.5 (0.88)	115	5.4	0.5 (0.80)	112
MO	1	9.1	0.3 (0.86)	117	7.6	0.3 (0.85)	126

Table 2. Characteristic dwell times of probes binding to Bvht H9 or Bvht H9:cs. $\tau_{unbound}$ is obtained from a single-exponential fit to the cumulative distribution of unbound dwell times. τ_{bound} is presented as a weighted average determined from a double-exponential fit to the cumulative distribution of bound dwell times, with the weight of the dominant component noted in parentheses. "N" indicates the number of single-molecule traces included in each condition.

Probe	$[Mg^{2+}]$ (mM)	T_M measured (°C)	T_M predicted (°C)
DNA	0	4.8*	4.1
DNA	1	7.2*	6.5
LNA2	0	16.9	5.4/18.8**
LNA2	1	19.4	7.8/21.5**
LNA23	0	20.2	9/22.4**
LNA23	1	20.9	11.5/21.5**
MO	0	17.6	-
MO	1	18.1	-

Table 3. T_M values for each probe type hybridized to Bvht H9 34-45 in the presence or absence of 1 mM $MgCl_2$. Predicted T_M values were obtained using IDT OligoAnalyzer. *Upper limit of T_M due to incomplete hybridization. **RNA target calculation setting/DNA target calculation setting.

		Bvht H9			Bvht H9:cs		
$[Mg^{2+}]$ (mM)	$[Na^{+}]$ (mM)	$\tau_{unbound}$ (s)	$\tau_{bound,avg}$ (s) (weight)	N	$\tau_{unbound}$ (s)	$\tau_{bound,avg}$ (s) (weight)	N
*0	100	9.9	0.1 (0.99)	101	3.7	0.6 (0.55)	104
*1	100	9.4	0.2 (1.00)	109	5.2	0.7 (0.55)	167
1	200	9.6	0.2 (1.00)	93	6.8	0.9 (0.51)	157
1	300	9.3	0.2 (1.00)	105	5.0	0.9 (0.54)	146
1	500	10.0	0.2 (0.94)	103	5.7	1.0 (0.51)	135
20	100	9.1	0.2 (1.00)	89	7.4	0.1 (0.89)	62

Table 4. Characteristic dwell times of LNA2 binding to Bvht H9 or Bvht H9:cs in indicated salt concentrations. $\tau_{unbound}$ is obtained from a single-exponential fit to the cumulative distribution of unbound dwell times. τ_{bound} is presented as a weighted average determined from a double-exponential fit to the cumulative distribution of bound dwell times, with the weight of the dominant component noted in parentheses. “N” indicates the number of single-molecule traces included in each condition.
*Data in these rows reproduced from Table 2 for ease of comparison

		Bvht H9			Bvht H9:cs		
$[Mg^{2+}]$ (mM)	$[Na^{+}]$ (mM)	$\tau_{unbound}$ (s)	$\tau_{bound,avg}$ (s) (weight)	N	$\tau_{unbound}$ (s)	$\tau_{bound,avg}$ (s) (weight)	N
*0	100	2.8	0.5 (0.88)	115	5.4	0.5 (0.80)	112
*1	100	9.1	0.3 (0.86)	117	7.6	0.3 (0.85)	126
1	500	7.7	0.3 (0.88)	113	7.5	0.3 (0.89)	135

Table 5. Characteristic dwell times of MO binding to Bvht H9 or Bvht H9:cs in indicated salt concentrations. $\tau_{unbound}$ is obtained from a single-exponential fit to the cumulative distribution of unbound dwell times. τ_{bound} is presented as a weighted average determined from a double-exponential fit to the cumulative distribution of bound dwell times, with the weight of the heavier component noted in parentheses. “N” indicates the number of single-molecule traces included in each condition.
*Data in these rows reproduced from Table 2 for ease of comparison

Figure Legends

Figure 1. *A*, Model RNA structures for probing with SiM-KARTS. The probe binding site is indicated in red. Complementary RNA strands stably bound to the primary RNA and fluorescently labeled with Cy3 are indicated in blue. Full structure of Bvht and location of H9 region are displayed in the upper right. *B*, Example image from SiM-KARTS data collection. RNA is detected in the left channel via Cy3 fluorescence from either the RNA or a complementary strand (here, 3' Cy3 cs), while the probe is detected in the right channel via Cy5 or TYE665 fluorescence (here, 5' TYE665 LNA2). *C*, Backbone chemistry and example single-molecule trace for a DNA probe binding to Bvht H9:cs. Top: HMM idealization of red channel (probe) trace. Middle: Red (probe) channel trace; Bottom: Green (RNA) channel trace. *D*, Backbone chemistry and example single-molecule trace for a DNA probe containing one LNA residue binding to Bvht H9:cs. *E*, Backbone chemistry and example single-molecule trace for a morpholino probe binding to Bvht H9:cs.

Figure 2. Probe identity affects lengths of RNA-bound and unbound dwells. *A*, Cumulative distributions of unbound dwell times obtained at 0 mM $MgCl_2$ for each probe type binding to Bvht H9 (dashed) and Bvht H9:cs (solid). *B*, Bound dwell times obtained at 0 mM $MgCl_2$ for each probe type binding to Bvht H9 and Bvht H9:cs. *C*, Unbound dwell times obtained at 1 mM $MgCl_2$ for each probe type binding to Bvht H9 and Bvht H9:cs. *D*, Bound dwell times obtained at 1 mM $MgCl_2$ for each probe type binding to Bvht H9 and Bvht H9:cs.

Figure 3. Melting curves for hybrids of each probe type and Bvht H9 34-45 measured by absorbance at 260 nm and rescaled to run from 0 to 1. *A*, Melting curves for each probe recorded at 0 mM $MgCl_2$. *B*, Melting curves for each probe recorded at 1 mM $MgCl_2$.

Figure 4. Impact of ionic concentration on dwell times of LNA2 binding to Bvht H9 (dashed) or Bvht H9:cs (solid). *A*, Cumulative distributions of unbound dwell times for LNA2 at 100 mM NaCl and varying $MgCl_2$ concentration. *B*, Bound dwell times for LNA2 at 100 mM NaCl and varying $MgCl_2$ concentration. *C*, Unbound dwell times for LNA2 at 1 mM $MgCl_2$ and varying NaCl concentration. *D*, Bound dwell times for LNA2 at 1 mM $MgCl_2$ and varying NaCl concentration.

Figure 5. Circular dichroism of RNA at varying $MgCl_2$ concentration. *A*, CD of Bvht H9 34-45 at indicated $MgCl_2$ concentrations. *B*, CD of Bvht H9:cs at indicated $MgCl_2$ concentrations.

Figure 6. Impact of ionic concentration on dwell times of MO binding to Bvht H9 (dashed) or Bvht H9:cs (solid). *A*, Cumulative distributions of unbound dwell times for MO at indicated combinations of NaCl and $MgCl_2$ concentration. *B*, Bound dwell times for MO at indicated combinations of NaCl and $MgCl_2$ concentration.

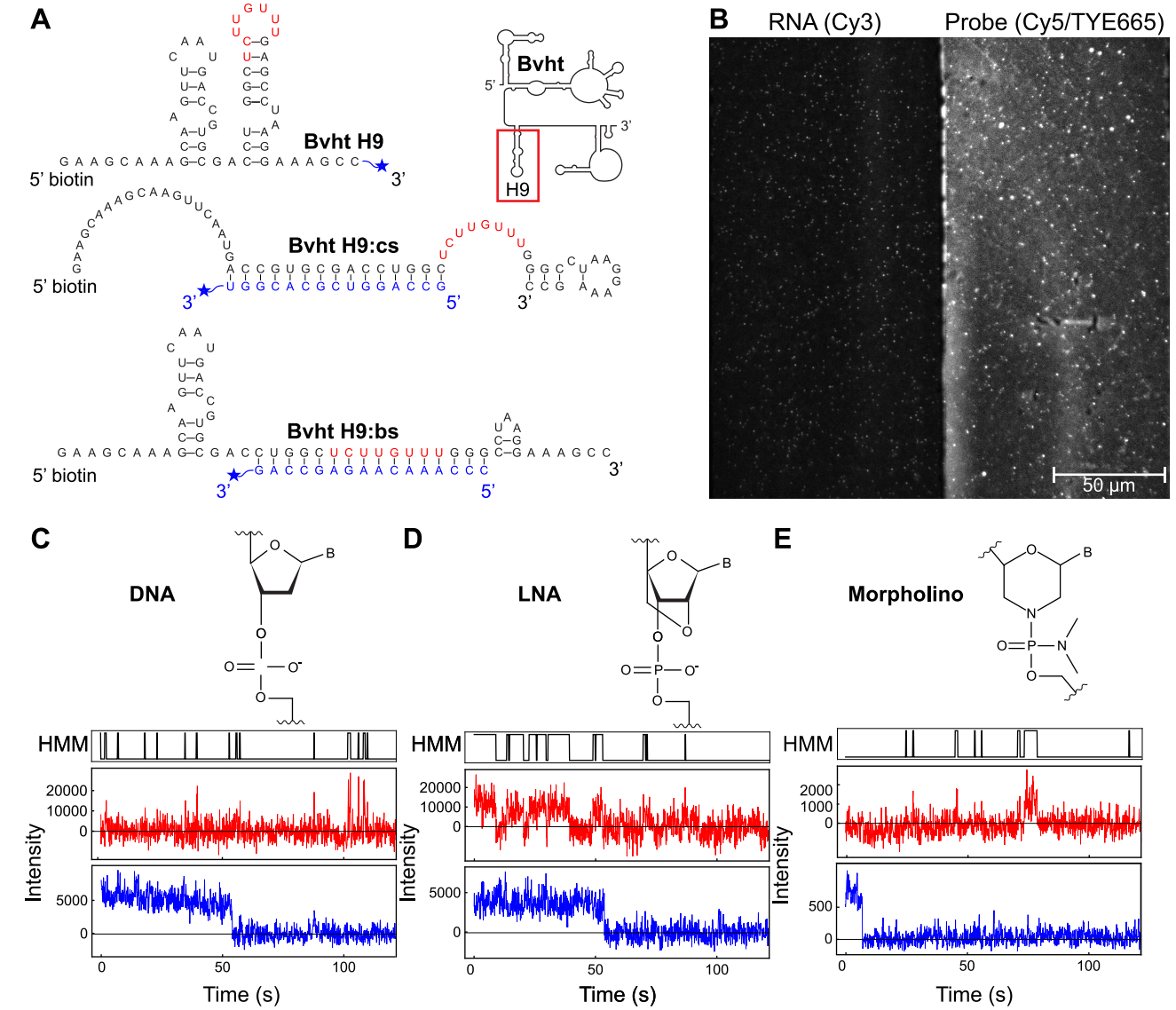
A
Bvht H9
5' biotin
3'
Bvht
5'
3'
H9
Bvht H9:cs
5' biotin
3'
5'
3'
Bvht H9:bs
5' biotin
3'
5'
3'
B
RNA (Cy3)
Probe (Cy5/TYE665)
50 µm
C
DNA
D
LNA
E
Morpholino
HMM
Intensity
Time (s)

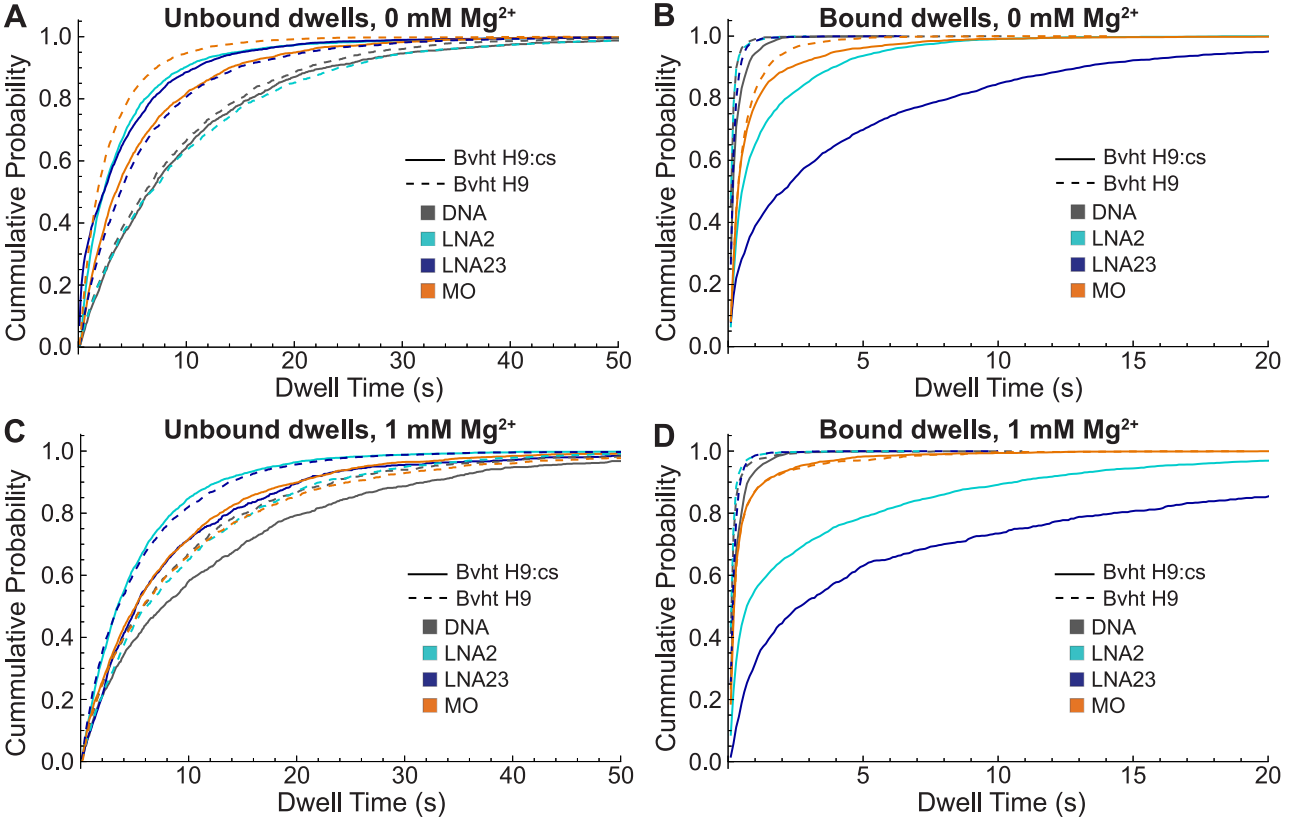
A
Unbound dwells, 0 mM Mg2+
B
Bound dwells, 0 mM Mg2+
C
Unbound dwells, 1 mM Mg2+
D
Bound dwells, 1 mM Mg2+
Cummulative Probability
Dwell Time (s)
Bvht H9:cs
Bvht H9
DNA
LNA2
LNA23
MO

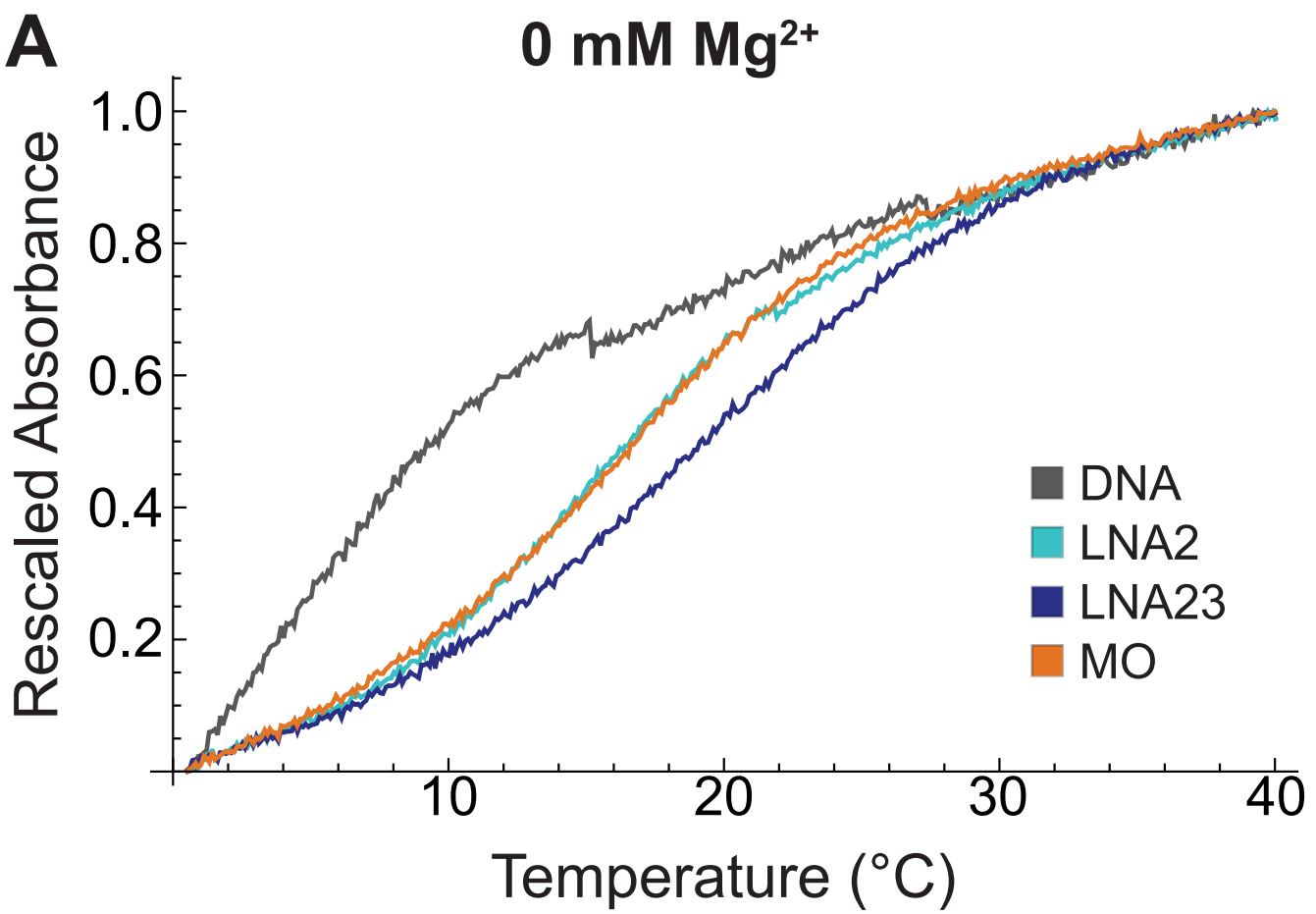
A
0 mM Mg2+
Rescaled Absorbance
1.0
0.8
0.6
0.4
0.2
10
20
30
40
Temperature (°C)
DNA
LNA2
LNA23
MO

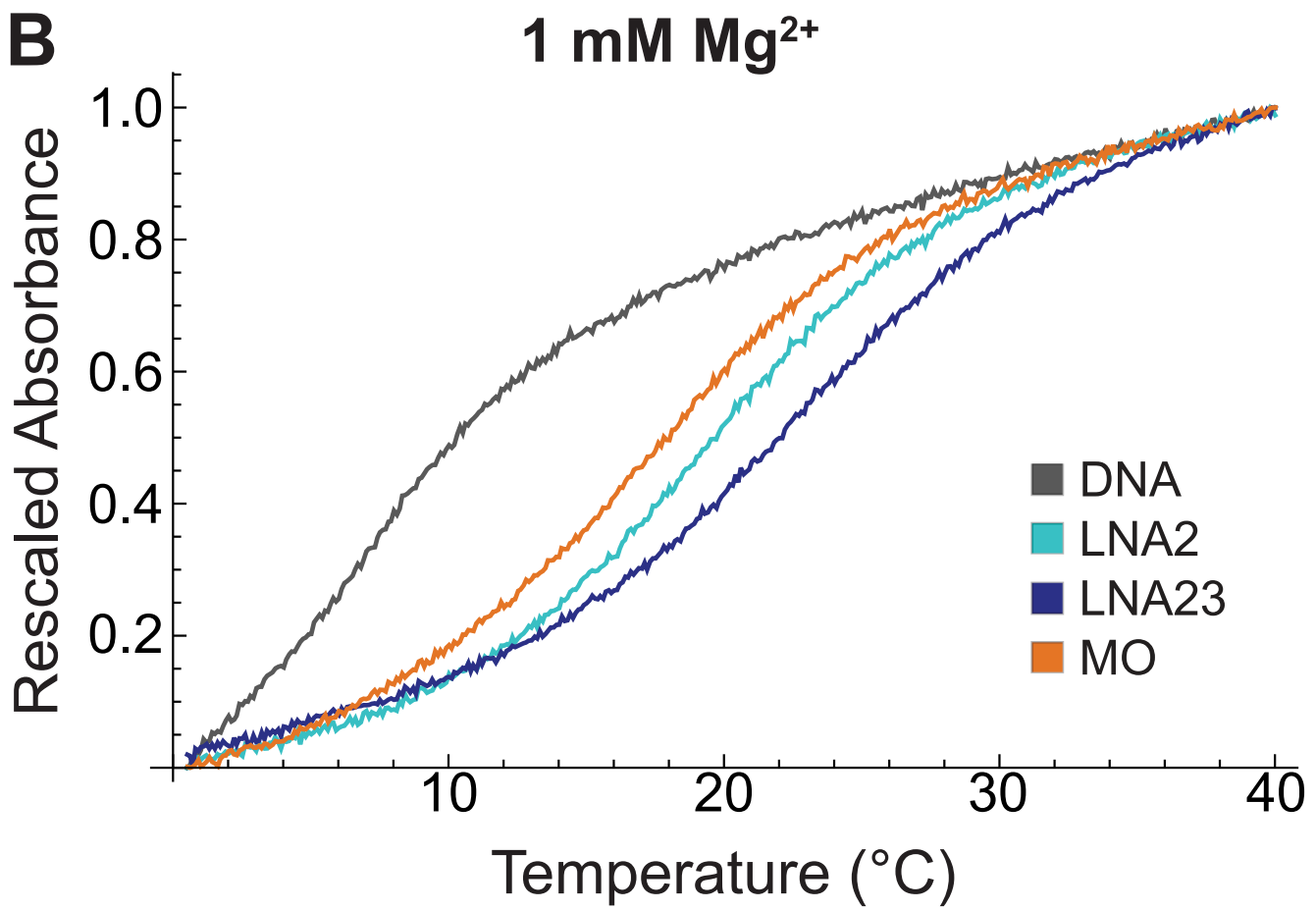
B
1 mM Mg2+
Rescaled Absorbance
1.0
0.8
0.6
0.4
0.2
10
20
30
40
Temperature (°C)
DNA
LNA2
LNA23
MO

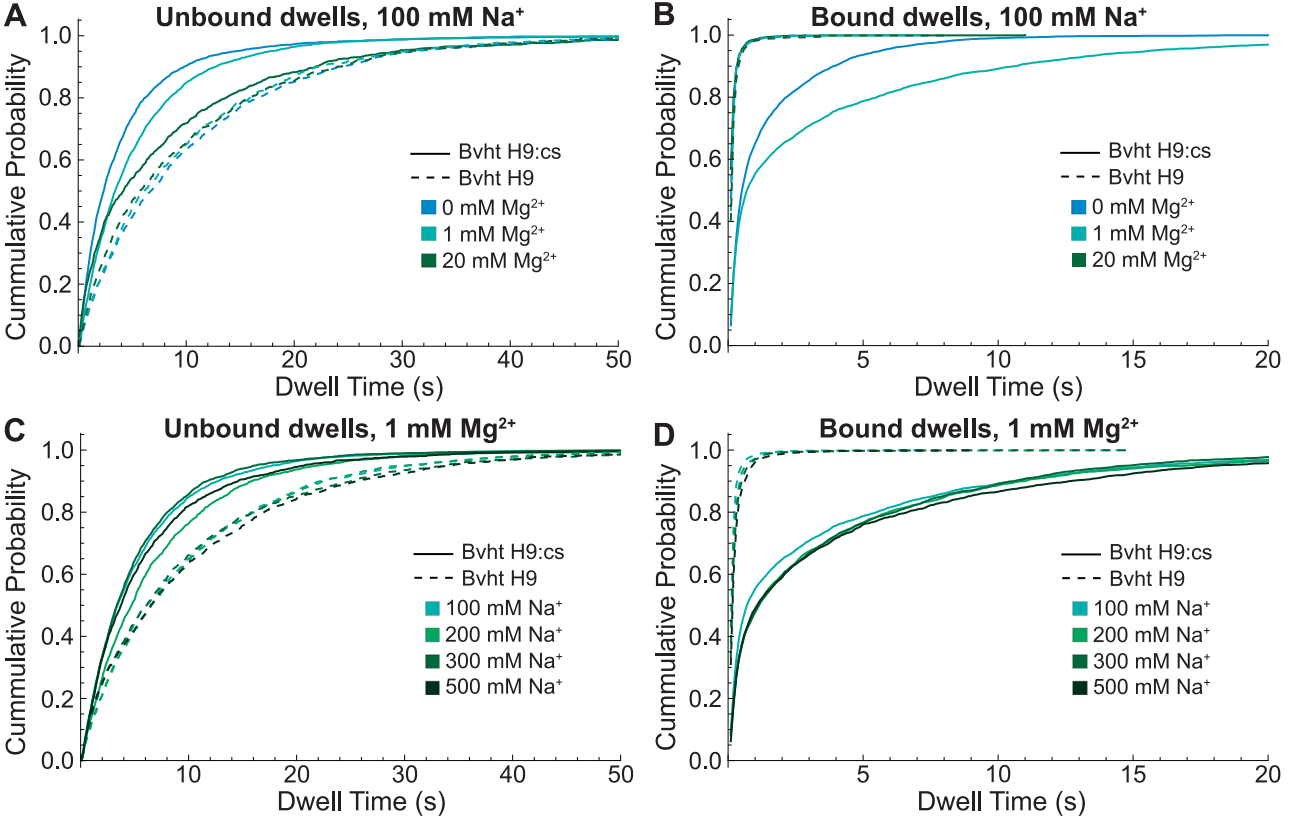
A
Unbound dwells, 100 mM Na+
Cummulative Probability
Dwell Time (s)
Bvht H9:cs
Bvht H9
0 mM Mg2+
1 mM Mg2+
20 mM Mg2+
B
Bound dwells, 100 mM Na+
Cummulative Probability
Dwell Time (s)
Bvht H9:cs
Bvht H9
0 mM Mg2+
1 mM Mg2+
20 mM Mg2+
C
Unbound dwells, 1 mM Mg2+
Cummulative Probability
Dwell Time (s)
Bvht H9:cs
Bvht H9
100 mM Na+
200 mM Na+
300 mM Na+
500 mM Na+
D
Bound dwells, 1 mM Mg2+
Cummulative Probability
Dwell Time (s)
Bvht H9:cs
Bvht H9
100 mM Na+
200 mM Na+
300 mM Na+
500 mM Na+

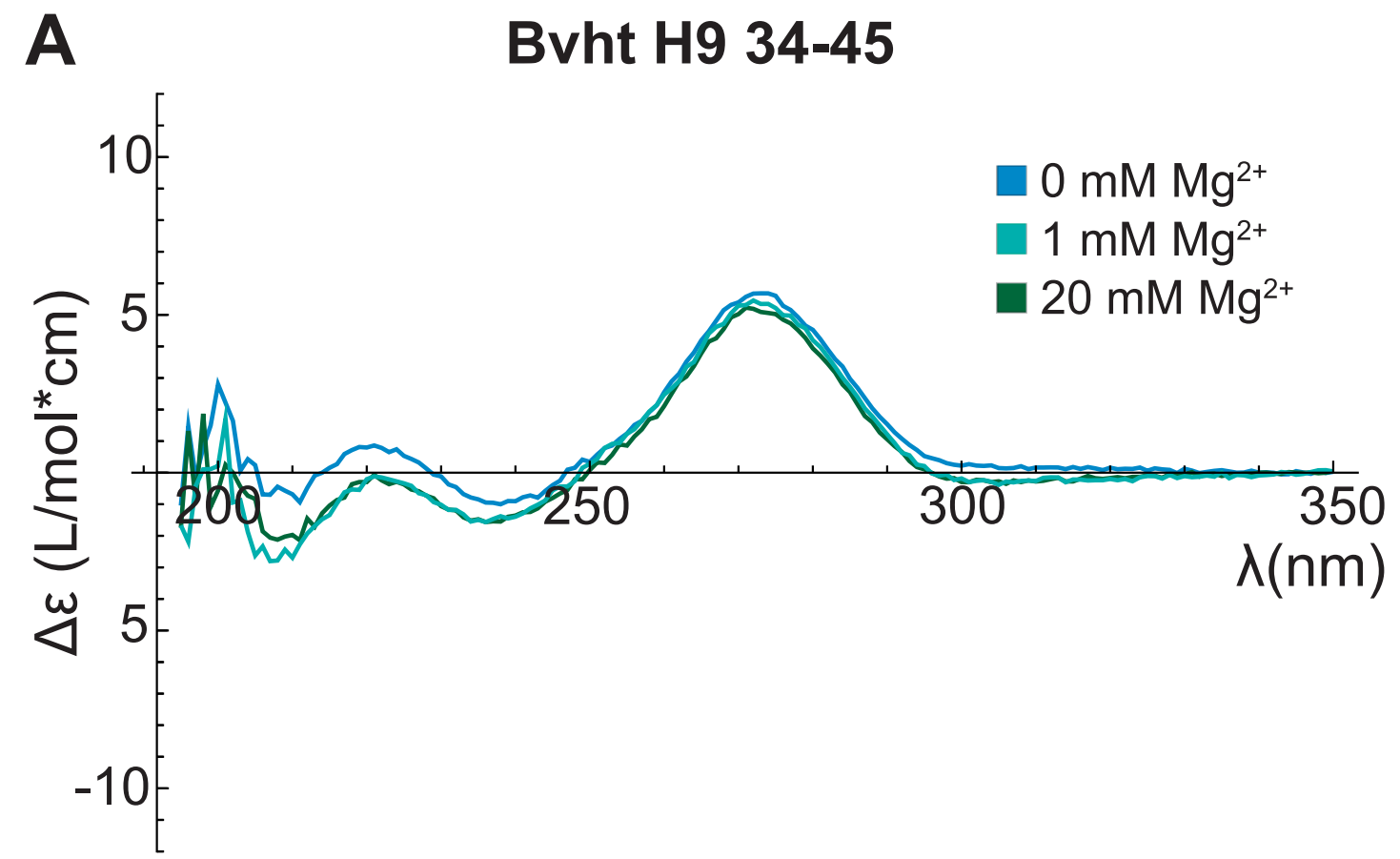
A
Bvht H9 34-45
10
5
-5
-10
Δε (L/mol*cm)
200
250
300
350
λ(nm)
0 mM Mg2+
1 mM Mg2+
20 mM Mg2+

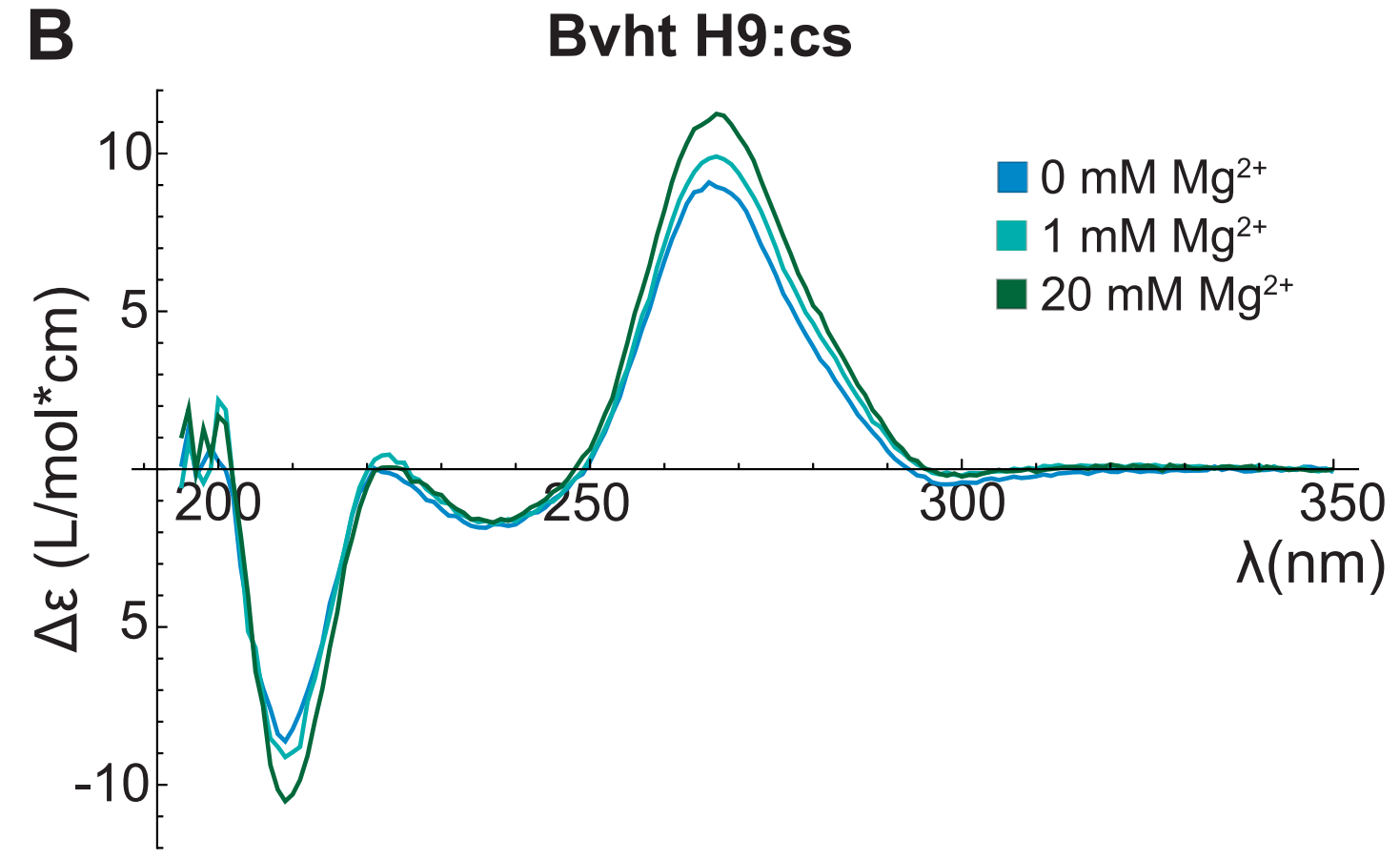
B
Bvht H9:cs
10
5
-5
-10
Δε (L/mol*cm)
200
250
300
350
λ(nm)
0 mM Mg2+
1 mM Mg2+
20 mM Mg2+

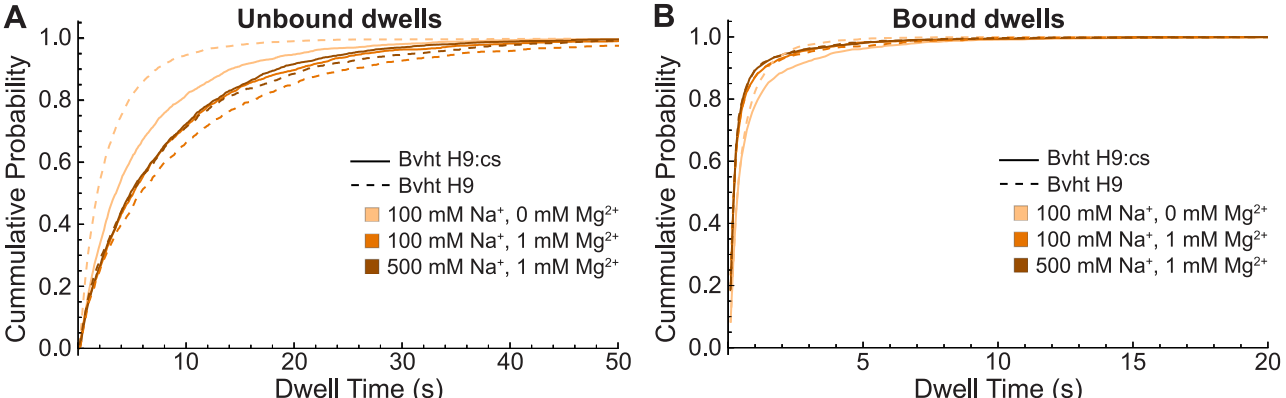
A
Unbound dwells
Cummulative Probability
Dwell Time (s)
Bvht H9:cs
Bvht H9
100 mM Na+, 0 mM Mg2+
100 mM Na+, 1 mM Mg2+
500 mM Na+, 1 mM Mg2+
B
Bound dwells
Cummulative Probability
Dwell Time (s)
Bvht H9:cs
Bvht H9
100 mM Na+, 0 mM Mg2+
100 mM Na+, 1 mM Mg2+
500 mM Na+, 1 mM Mg2+